Statistical Study on the Nature of Solar-Flux Emergence

Kenichi Otsuji,[1,2] Reizaburo Kitai,[2] Kiyoshi Ichimoto,[2] and Kazunari Shibata[2]

[1]*National Astronomical Observatory of Japan, 2-21-1 Mitaka, Tokyo 181-8588*
otsuji@solar.mtk.nao.ac.jp
[2]*Kwasan and Hida Observatories, Kyoto University, Yamashina-ku, Kyoto 607-8741*

Abstract

We studied 101 flux emergence events ranging from small ephemeral regions to large emerging flux regions that were observed with the Hinode Solar Optical Telescope filtergram. We investigated how the total magnetic flux of the emergence event controls the nature of emergence. To determine the modes of emergences, horizontal velocity fields of the global motion of the magnetic patches in the flux emerging sites were measured by local correlation tracking. Between two main polarities of the large emerging flux regions with more than around 2×10^{19} Mx, there were converging flows of anti-polarity magnetic patches. On the other hand, small ephemeral regions showed no converging flow, but a simple diverging pattern. When we looked into the detailed features in the emerging sites, irrespective of the total flux and the spatial size, all of the emergence events were observed to consist of single or multiple elementary emergence unit(s). The typical size of unitary emergence is 4 Mm, and consistent with simulation results. From a statistical study of the flux emergence events, the maximum spatial distance between two main polarities, the magnetic flux growth rate and the mean separation speed were found to follow the power-law functions of the total magnetic flux with indices of 0.27, 0.57, and -0.16, respectively. From a discussion on the observed power-law relations, we obtained a physical view of solar flux emergence, in which the emerging magnetic fields float and evolve while balancing to the surrounding turbulent atmosphere.

Key words: Sun: chromosphere — Sun: emerging flux — Sun: magnetic fields — Sun: photosphere

1. Introduction

The sites where the subsurface magnetic flux tubes emerge on the solar surface are called emerging flux regions (Bruzek 1969; Zirin 1972). The typical simple emerging flux region has one main pair of opposite magnetic concentrations at both ends of the emerging site. The opposite magnetic concentrations of the main pair move away from each other with a speed of 1–2 km s^{-1} (Zwaan et al. 1985; Brants 1985) in the developing phase of the region. Inside the developing emerging site there are many magnetic flux tubes emerging on the photosphere. The newly emerged magnetic flux tubes at the emerging site appear as dark granular lanes (Loughhead & Bray 1961; Brants & Steenbeek 1985) on the photosphere. At both ends of the dark granular lane, there are the magnetic concentrations, which are called footpoints, and are observed as bright points in the G-band image (Otsuji et al. 2007). With Hα the emerged flux tubes are observed as dark arch filaments (Bruzek 1967). The lifetime of an arch filament is 10–30 min (Bruzek 1967; Chou & Zirin 1988). The rise velocity of arch filaments is 10–15 km s^{-1} (Bruzek 1969; Chou & Zirin 1988). Otsuji et al. (2010) found the deceleration of the apex of the small-scale arch filaments in the chromosphere.

Emerging flux regions show a variety of size, lifetime, total magnetic flux, and field strength. Especially the small emerging flux regions are called the ephemeral active region (EAR: Harvey & Martin 1973). For convenience, on the following pages we define larger (i.e., non-EAR) emerging flux regions as EFRs. EFRs are produced by fairly large-scale flux emergence. They have a pair or a more complex group of

sunspots with definite penumbrae. The typical size of EFRs is more than 30 Mm (Bruzek 1967). EFRs show their emergence activities for several days, and exist on the solar surface for a few months at the maximum. The total flux in an EFR increases with a rate of 10^{20} Mx hr^{-1}, and reaches to the order of 10^{20}–10^{22} Mx (Zwaan 1987). In a fairly developed EFR, the field strength of the main spot is around 3000 gauss (Brants & Zwaan 1982).

EARs have a simple bipolar configuration. They have no penumbra in the sunspots. The typical size varies from 5 Mm to 30 Mm (Harvey & Martin 1973; Harvey et al. 1975; Hagenaar 2001; Otsuji et al. 2007). EARs have a short lifetime of hours, or one day. The total flux in an EAR is up to 10^{20} Mx with an increase rate of 10^{19} Mx hr^{-1}. The magnetic field strength of the main spot is from a few times 100 gauss (Martin 1988) to 2000 gauss (Brants & Zwaan 1982).

Various simulation studies on flux emergence have been performed by many researchers (Shibata et al. 1989; Matsumoto & Shibata 1992; Fan 2001). They showed simple bipolar emergence simulations that correspond to the observation result. Matsumoto et al. (1993) and Magara and Longcope (2001) simulated the three-dimensional magnetohydrodynamics (MHD) of the emerging magnetic flux. Nozawa (2005) and Murray et al. (2006) also performed MHD simulations of flux emergence with the sheared or twisted flux tube. They found that the flux tube with shear or twist emerges faster than that without any shear and twist.

Nozawa et al. (1992) performed MHD simulations of flux emergence in a sheet geometry. The initial stable flux sheet in the convective zone was perturbed with various wavelengths,

which correspond to the convective motion. They found that irrespective of the wavelength of the initial perturbation, a finite "most unstable wavelength" is excited. This wavelength (2–4 Mm) is inherent in the Parker instability (Parker 1966). As a result, the flux sheet is undulated and the apexes of the convex field line (Ω-loops) appear consecutively on the photosphere. Some of the dipped field lines (U-loops) also emerge to form regions called "bald patches (Titov et al. 1993)".

On the other hand, an observational study on a large EFR and bald patches was performed by Pariat et al. (2004). They observed a fairly large ($\sim$30 Mm) EFR with the magnetogram, and found that the emerged field lines undulate vertically. They revealed that there are many bald patches between the main spots. These results confirmed that the emerging flux tube does not rise altogether at a time, but each Ω-loop component rises individually. They proposed this model as a "resistive emergence model". The distance between two consecutive bald patches is in the range of 2–6 Mm, which is consistent with a theoretical argument on the flattening of the emerging magnetic field just below the surface and its critical emergence length, first presented by Magara (2001).

Recently, Isobe et al. (2007) further developed the simulation performed by Nozawa et al. (1992), and obtained results in which the undulated field line caused reconnections with neighboring Ω-loops, and created larger loops. Archontis and Hood (2009) performed three-dimensional MHD simulations of the emergence of undulating fieldlines. These reconnection events are interpreted as being sources of Ellerman bombs (Ellerman 1917; Kurokawa et al. 1982; Kitai 1983; Matsumoto et al. 2008a, 2008b; Watanabe et al. 2008).

The resistive emergence model is applicable to the large EFR. Furthermore, recently Otsuji et al. (2007) found bald patches inside a small-scale EAR ($\sim$5 Mm) using Solar Optical Telescope (SOT: Ichimoto et al. 2004; Tsuneta et al. 2008; Suematsu et al. 2008; Shimizu et al. 2007) aboard Hinode (Kosugi et al. 2007). However, Centeno et al. (2007) and Guglielmino et al. (2008) showed small EARs (2 Mm and 6 Mm, respectively) without an undulated magnetic field.

As stated above, the criteria of bald patches formation are still uncertain. Furthermore, in the latest simulation, the footpoints of emerged flux loops showed converging motion toward the bald patches on the photosphere (Cheung et al. 2010). Although this converging motion was observed in preceding studies (Strous et al. 1996; Strous & Zwaan 1999; Bernasconi et al. 2002; Cheung et al. 2008), a statistical analysis on that phenomenon with respect to the size and magnetic characteristics of the flux emergences has not yet been done.

To clarify the criteria of forming a bald patch and converging flow, we performed a statistical study about the nature of magnetic flux emergences using SOT. The flux emergence phenomena from small EARs to large EFRs observed by SOT were investigated concerning their morphological and magnetical characteristics. Furthermore, we derived relations between the total magnetic flux and the maximum spatial size, the flux growth rate and the mean separation speed of the emergence event in order to clarify how the total flux amount controls the entire evolution of the emergence.

2. Observation and Data Reduction

2.1. Observation and Data Selection

Hinode satellite has observed the solar surface for over 4 years with SOT. SOT has Broadband Filter Imager (BFI) and Narrowband Filter Imager (NFI). Ca II H (3968.5 Å) filtergrams were taken by BFI with the bandpass of 3 Å. Fe I (6302 Å) and Na I D (5896 Å) polarimetric data in the solar photosphere and chromosphere were observed with NFI. To search for emerging flux phenomena, we used Hinode daily quicklook movies.[1] Among the possible candidates, we selected 101 emerging flux phenomena according to the criteria as follows: (1) conspicuous presence of separating bright points in Ca II H image and/or opposite polarities in Fe I or Na I D image, (2) location fairly inside the solar limb [$\alpha = \arcsin (r/R) \leq 70°$, where r is the distance from solar disk center to the location of the event and R is the solar radius], (3) observational time span longer than 1 hour, and (4) observational cadence higher than
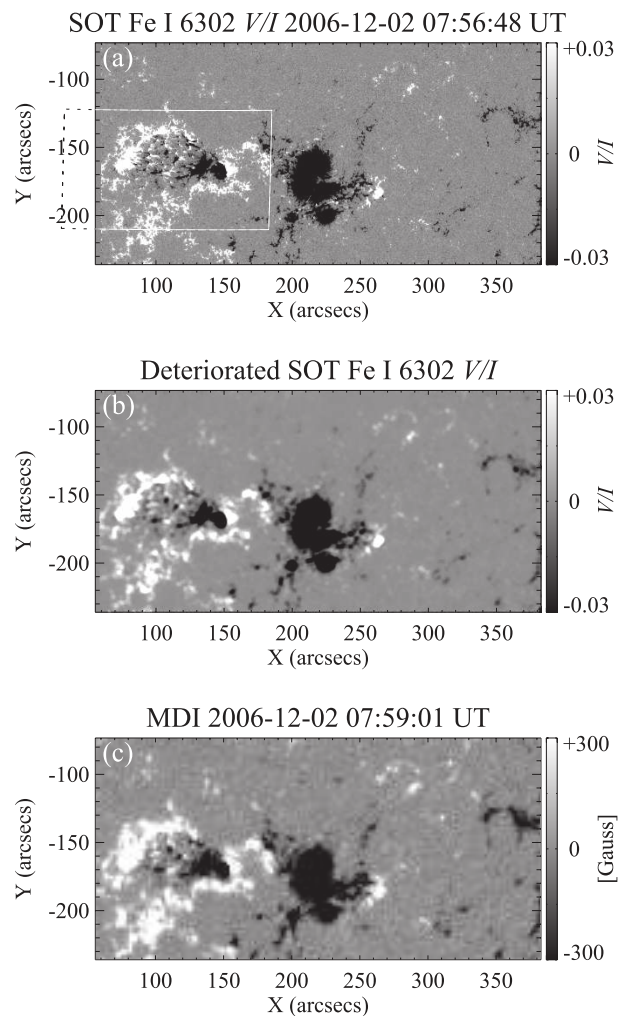

Fig. 1. (a) Pointing-corrected SOT polarimetric image with the white box indicating the area of the "top-view image" in figure 4. (b) Deteriorated SOT polarimetric image. (c) Reference SOHO MDI image estimated by linear interpolation.

---

[1] ⟨http://hinode.nao.ac.jp/QLmovies/⟩.

SOT V/I vs. MDI magnetogram

Correlation coefficient=0.95
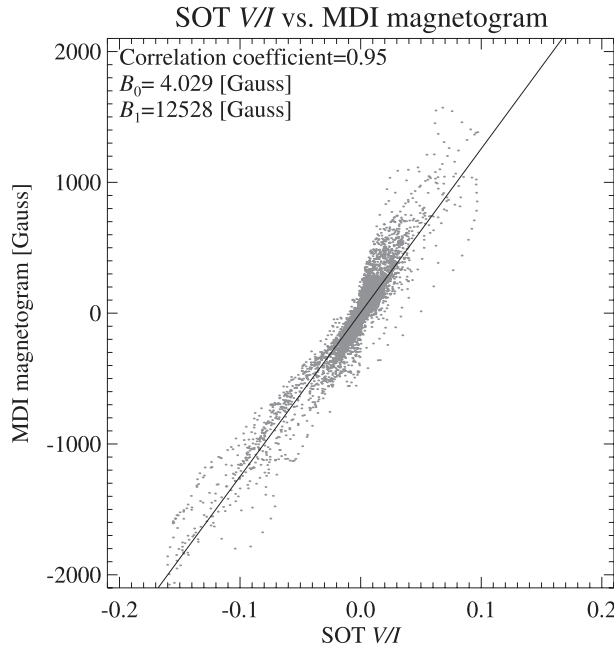B_0= 4.029 [Gauss]
B_1=12528 [Gauss]

Fig. 2. Scatter plot of the polarimetric signal V/I of SOT and the field strength of the MDI magnetogram.

10 minutes. The period with which we studied was between 2006 November 26 to 2010 August 23. Detailed observational information of the emerging flux is available in associated electronic tables.[2]

2.2. Data Reduction

In this section we give a description of the data reduction with the data of EFR 20061201 (# 2 in the electronic table, figure 1) as an example. First, dark-current subtraction and flat fielding were performed on the obtained SOT data in the standard manner. We then processed every observed data, as described below.

First, we used the SOHO-Michelson Doppler Imager (MDI: Scherrer et al. 1995) magnetogram data to calibrate SOT polarimetric data. We compensated the differential rotation of two consecutive MDI data observed before and after the SOT observation, and interpolated them by time to estimate the distribution of the magnetic field at the time of the SOT observation. Next, we deteriorated the SOT polarimetric data with the spatial resolution of the MDI magnetogram (2″). Using the deteriorated SOT polarimetric data and the MDI magnetogram, we made a scatter plot of the SOT polarimetric signal (Stokes V/I) to the MDI field strength (figure 2). The correlation coefficient of SOT V/I to the MDI field strength was 0.95. We performed a linear fitting on the scatter plot, and obtained the conversion equation from SOT V/I to the photospheric field strength B_p, expressed as

$$B_p = B_1 \times V/I + B_0. \tag{1}$$

In the case of figure 2, the offset value, B_0, and the scaling factor, B_1, were 4.029 gauss and 12528 gauss, respectively.

---

[2]   Available at ⟨http://pasj.asj.or.jp/v63/n5/630521/⟩.

Note that the scatter of the data points in the figure is mainly due to the Doppler effect arising from the satellite's orbital motion. With this method we converted the SOT polarimetric signals to the magnetic flux densities for all samples.

In measuring the actual size of the solar features, we compensated the projection effect. We then applied the subsonic filter for 3 minutes to the SOT Ca II H image sequence in order to suppress chromospheric oscillatory motions (figure 3b).

3. Analysis

As stated in the introduction, mutually approaching anti-polarity patches were observed in undulating resistive emerging phenomena (Strous & Zwaan 1999). We studied the formation process of the converging motion between the opposite polarities in EFR and EAR by analysing the morphological, dynamical and magnetic evolutions of our SOT samples. In this section we introduce our analysis methods using the data of EFR 20061201.

3.1. Morphological Evolution

The morphological evolution of the magnetic flux emergence was analysed by two methods. One was the method of tracking magnetic elements using local correlation tracking (LCT), and the other using time-sliced diagram.

3.1.1. Local correlation tracking

The local correlation tracking (LCT) method is commonly used to derive the horizontal velocity field (November & Simon 1988; Berger et al. 1998; Matsumoto & Kitai 2010). For LCT, we used `flowmap.pro` in SSW of IDL. `Flowmap.pro` calculates the two-dimensional vector flowfield by following the subtiles in the time series of two-dimensional images.

To examine the motion of the footpoints of flux tubes for all over the emerging site, we performed LCT on SOT magnetogram data and obtained the velocity field of moving magnetic elements (figure 3c). The size of tracking subtile for LCT was 0″.5. To reduce the velocity noise due to the LCT error, the velocity fields were averaged both spatially and temporally over zones of 1″ × 1″ and 10 minutes, respectively. The standard deviation of the velocity field inside the data cube of 1″ × 1″ × 10 min was ∼0.1 km s^{-1}.

We then derived the divergence of the horizontal velocity field (figure 3d). To emphasize the global and sustained flows, the divergence maps were averaged both spatially and temporally. The spatial average was performed with a width of 10″ for large EFR and 3″ for small EAR. The threshold between large EFRs and small EARs was fixed to be 40″, which is the upper-limit size of ephemeral active regions indicated by Harvey and Martin (1973). For EFR 20061201, the spatial averaging box size was 10″. The temporally averaging period was taken as 10 minutes for all events.

3.1.2. Time-sliced diagram

To clarify the dynamics of footpoints more quantitatively, we made a time-sliced diagram of SOT magnetograms (figure 3e). The spatial slit was located parallel to the axis of the EFR (shown in figure 3a). From the time-sliced diagram, we derived the maximum distance, d_{max}, between the main spots, the mean separating speed $\langle v \rangle$ of the main spots.
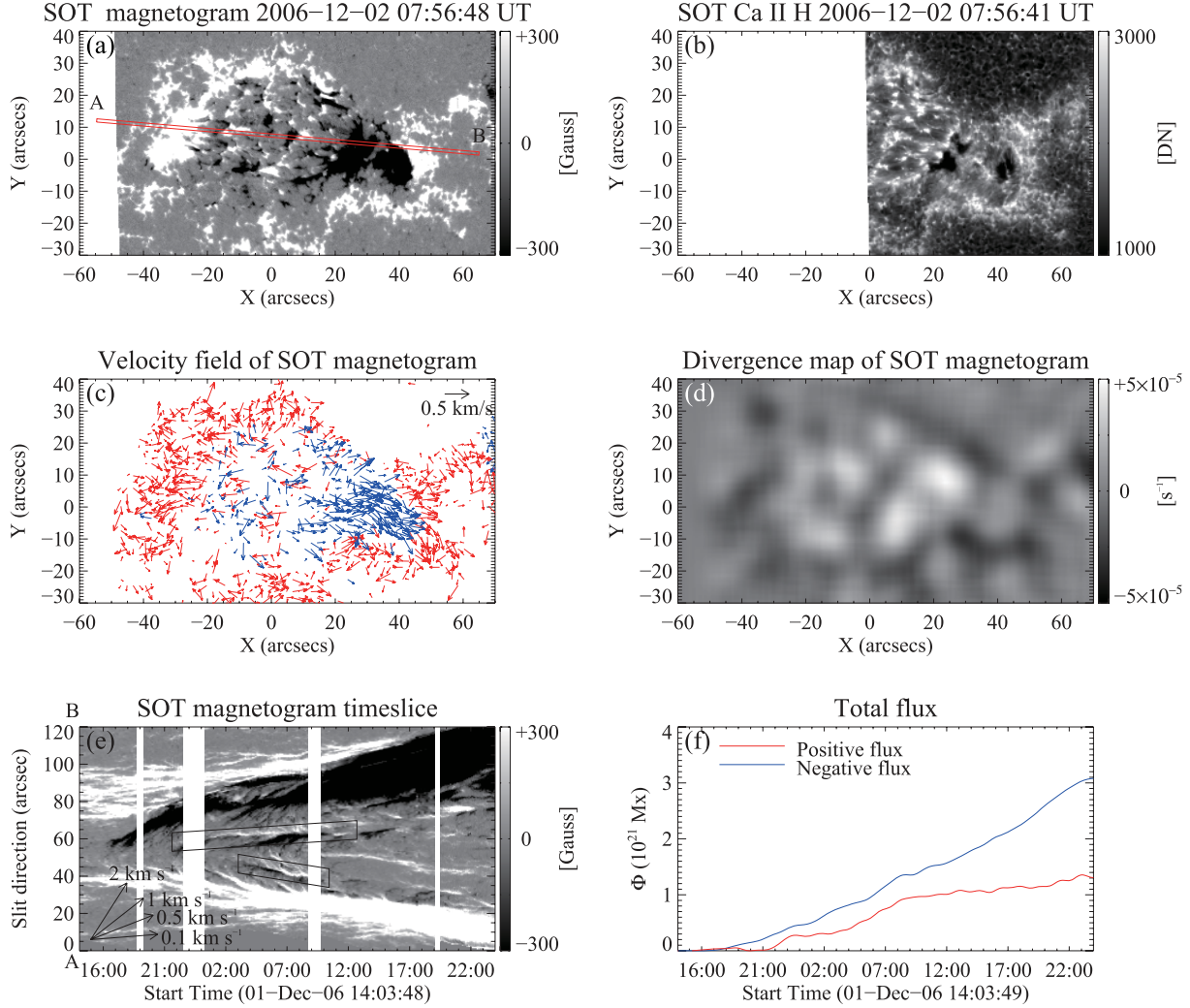
Fig. 3. EFR 20061201. (a) SOT Fe I magnetogram. (b) SOT Ca II filtergram. (c) Horizontal velocity field of magnetogram derived by LCT, averaged with 1″ and 1 minute. Red and blue arrows indicate the velocities of positive and negative magnetic components. The threshold field strength of drawing arrows is ± 50 gauss. (d) Divergence map derived from the horizontal velocity field. The spatially averaging width is 10″. The temporally averaging period is 10 minutes. (e) Time-sliced diagram of SOT magnetogram. Both edge of the slit (A and B) in panel (a) correspond to 0″ and 120″ in the plot, respectively. The vertical white gaps represent the observation breaks. The mutually approaching anti-polarities are indicated by black boxes. (f) Evolution of magnetic flux of the EFR.

Detailed footpoints motions, such as mutually approaching anti-polarities, were examined in this diagram.

3.2. Temporal Evolution of Magnetic Field

To investigate the temporal evolution of the emerging magnetic flux, we measured the total flux within the emerging site. Positive and negative fluxes were summed up separately. The total flux of the emerging region, Φ, was derived by subtracting the fluxes at the initial time. We plotted the variation of the positive and negative fluxes, respectively (figure 3f). From this plot, we derived the maximum amount of the unsigned total magnetic flux, Φ_{max}, and the unsigned flux growth rate, $\langle d\Phi/dt \rangle = \Phi_{max}/T$. The growth rate is defined as the total magnetic flux, Φ_{max}, divided by the continuously emerging period, T. Note that the unbalance between the positive and negative fluxes in the sample plot was due to the flow of positive flux out of the field of view.

4. Results

First, we introduce the sample results for large EFR and small EAR described in subsections 4.1 and 4.2, respectively. Then, the statistical results are shown in subsection 4.3.

4.1. Large EFR 20061201

In figure 3a, there are two main spots aligned in the east-west direction. The size of the main spots was 10″–20″. The field strength of the spots was $\pm 1.8 \times 10^3$ gauss at the maximum. Although the following spot is missing in the Ca II H image because of the field-of-view limitation (figure 3b), there are sunspots located at the same position with the preceding negative spots in the magnetogram. The velocity field shows prominent outward motions of the main spots (figure 3c). There are positive divergence areas inside the main spots (figure 3d), which indicate the flux emergences.
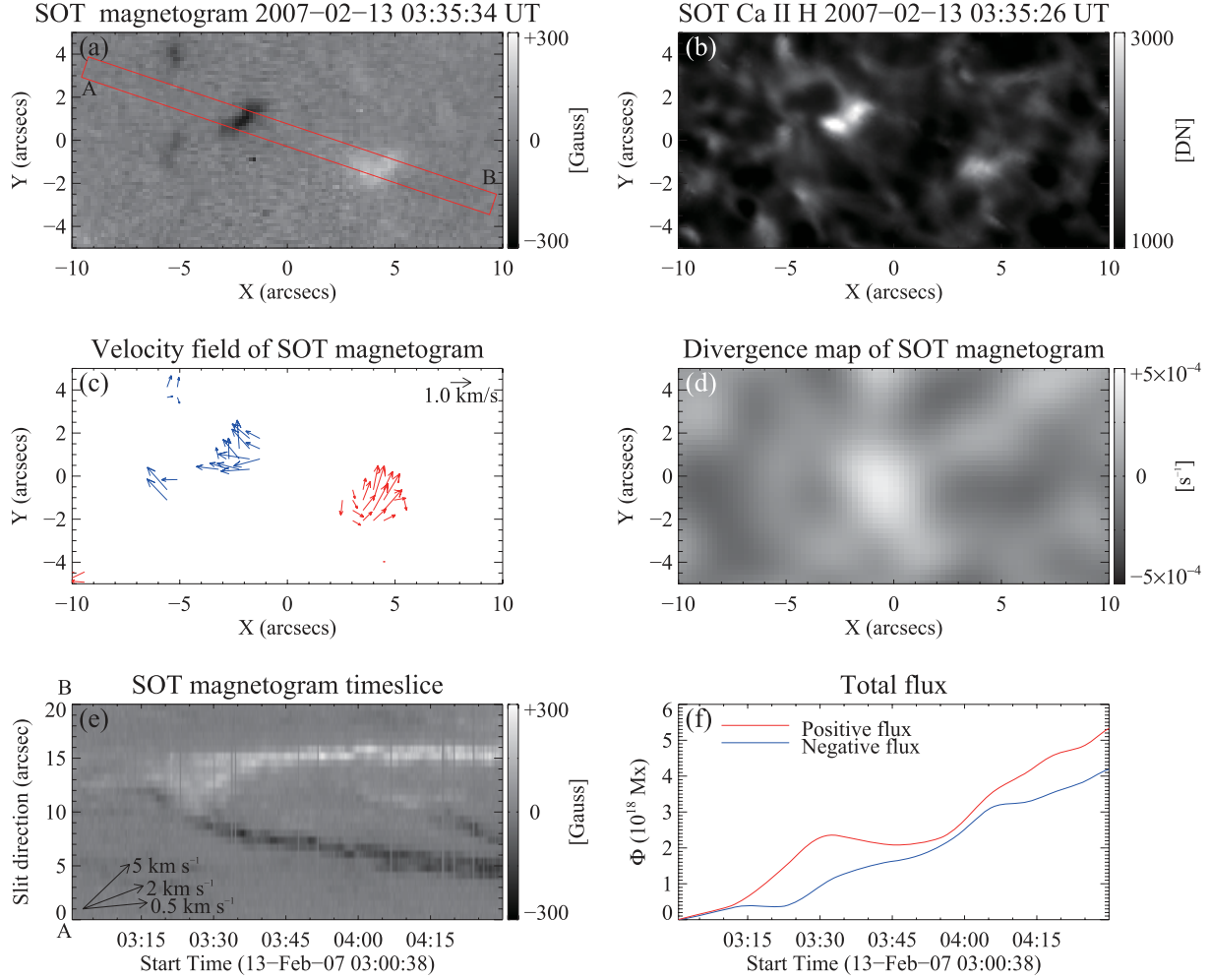
SOT magnetogram 2007−02−13 03:35:34 UT

SOT Ca II H 2007−02−13 03:35:26 UT

Velocity field of SOT magnetogram

Divergence map of SOT magnetogram

SOT magnetogram timeslice

Total flux

Fig. 4. EAR 20070213. (a) SOT Fe I magnetogram. (b) SOT Ca II filtergram. (c) Horizontal velocity field of magnetogram derived by LCT, averaged with $1''$ and 1 minute. Red and blue arrows indicate the velocities of the positive and negative magnetic components. The threshold field strength of drawing arrows is ± 50 gauss. (d) Divergence map derived from the horizontal velocity field. The spatially averaging width is $3''$. (e) Time-sliced diagram of SOT magnetogram. Both edges of the slit (A and B) in panel (a) correspond to $0''$ and $20''$ in the plot, respectively. (f) Evolution of the magnetic flux of the EAR.

From a time-sliced diagram (figure 3e), we can estimate the speed of the main spots to be $\sim 0.3\,\mathrm{km\,s^{-1}}$ for each; thus, the mean separating speed, $\langle v \rangle$, is about $0.6\,\mathrm{km\,s^{-1}}$. At the end of the observation period, the distance between two main spots increased to around $100''$. We considered this value to be the maximum distance, $d_{\max}$. The emergence started at 16:00 UT on December 1, and lasted until the observation end at 24:00 UT on December 2. Thus, the active emergence period was taken as 32 hours. The maximum amount of total magnetic flux was 1.3×10^{21} Mx for positive polarity and 3.1×10^{21} Mx for negative polarity (figure 3f). As the following positive spot flowed out of the field of view, the measured positive flux was less than that of the negative one. Thus, we took the maximum negative flux to be $\Phi_{\max}$. The mean flux growth rate, $\langle d\,\Phi/dt \rangle$, for this event was $9.7 \times 10^{19}\,\mathrm{Mx\,hr^{-1}}$.

Let us look at the central part of the region where there are many small positive or negative magnetic patches (figure 3a). These patches correspond to the Ca II H bright points (figure 3b). Although the magnetic patches seem to move with apparently random velocities in figure 3c, these patches are located in the converging region of the divergence map (figure 3d). Thus, these magnetic patches accumulated and stagnated to the localized area. In fact, the time-sliced diagram shows that these magnetic patches actually approach to each other with a speed of $\sim 1\,\mathrm{km\,s^{-1}}$. We thus identify these mutually approaching area as a U-loop formation in the EFR. In the following, we denote the area as the "stagnation zone (SZ)", where the anti-polarities mutually approach and accumulate.

4.2. Small EAR 20070213

We selected a small-scale magnetic emergence event that emerged on 2007 February 13 (# 9 in the electronic table) as the sample case of EAR. Figure 4a shows a magnetogram of this region. Two magnetic concentrations in the magnetogram correspond to the Ca II H bright points in figure 4b.

The field strength of the two magnetic concentrations was ± 300 gauss at the maximum. The velocity field of the small EAR shows separative and anti-clockwise rotational motion of two magnetic concentrations (figure 4c). Figure 4d is a divergence map derived from the velocity field and averaged spatially with $3''$. The divergence map shows the positive area at the central region of the EAR, which indicates that there is no converging flow inside the emerging site. In the time-sliced diagram we can see simple separating motion of two main magnetic concentrations and no stagnation zone (figure 4d). The maximum distance between the main concentration, d_{max}, was $10''$. The mean speed of the separating motion for main the concentrations, $\langle v \rangle$, is about $1.5\,\mathrm{km\,s^{-1}}$. The temporal evolution of the total flux shows that the maximum amounts of total fluxes are $5.4 \times 10^{18}\,\mathrm{Mx}$ for positive polarity and $4.2 \times 10^{18}\,\mathrm{Mx}$ for negative polarity (figure 4f). We took the maximum positive flux as Φ_{max} for this event. The time-sliced diagram and the total fluxes evolution plot indicate that the flux emergence began at 03:15 UT, and lasted until the observation end at 04:30 UT. Thus the active emergence period was 75 minutes, and the mean flux growth rate $\langle d\Phi/dt \rangle$ was $4.3 \times 10^{18}\,\mathrm{Mx\,hr^{-1}}$.

4.3. Statistical Result

Table 1 in Appendix gives the measured quantities of all samples. If there was no magnetic observation, Ca II H data were used to derive d_{max} and $\langle v \rangle$, and to judge the existence of SZs. There is no data of the total flux Φ_{max} and the flux growth rate $\langle d\Phi/dt \rangle$ for observations without the magnetogram. Figure 5 shows the statistical characteristics of the measured quantities.

4.3.1. Existence of SZ

In figure 5a, the histogram of the maximum separation distance, d_{max}, indicates that SZs are rarely found in small d_{max} regions. The flux emergence phenomena with a separation size of more than 25 Mm always have SZs. Below the threshold of 25 Mm, there are both EFRs and EARs with/without SZs. To clarify the conditions to have SZs, we categorized all of the events to three groups as follow. Group I: maximum separation distance of $d_{\mathrm{max}} \geq 25$ Mm and with SZs. Group II: maximum separation distance of $d_{\mathrm{max}} < 25$ Mm and with SZs. Group III: maximum separation distance of $d_{\mathrm{max}} < 25$ Mm and without SZ. Group I, II, and III are indicated in figure 5 by white, gray and black bars/squares, respectively. Figure 5b shows the histogram of the maximum fluxes, Φ_{max}, where we present the maximum flux separately for these three groups. Group I has a maximum flux of $\Phi_{\mathrm{max}} \sim 10^{21}$ Mx, while groups II and III have $\Phi_{\mathrm{max}} \sim 10^{20}$ Mx and $\sim 10^{19}$ Mx, respectively. Figure 5c shows the relation between the maximum flux, Φ_{max}, and the maximum separation distance, d_{max}. In the plot, the three groups I, II, and III are clearly separated. The maximum separation distance, d_{max}, depends on the maximum flux amount, Φ_{max}. The scatter plot implies a power-law relation of

$$d_{\mathrm{max}} = 7.9 \times 10^{-5} \Phi_{\mathrm{max}}^{0.27}, \tag{2}$$

where d_{max} is in Mm and Φ_{max} is in Mx. We can see a trend in which the small EARs have low values of maximum flux, while large EFRs have high values of maximum flux.

The power-law relation is consistent with the result of Hagenaar (2001), although the index of power was 0.18 instead of 0.27. From the result of categorization, we found that the SZ features are associated with a magnetic flux emergence of more than around 2×10^{19} Mx.

4.3.2. Size of elementary flux emergence

We also measured the typical size of elementary structures of emergence, d_{unit}, defined as the distance between two footpoints of individual Ω-loops at their emergence period. Some small footpoints of emerged loops might be finally transported to the border of supergranules by local convection. Others cause cancellation between the opposite polarities and disappear, which enlarges the distance between two footpoints of individual Ω-loops, (i.e., d_{unit}). Thus, the d_{unit} varies with time. For the accurate descriptions, we adopted the d_{unit} at the epoch when the Ω-loops were observed as Ca II H filaments (~ 10 minutes after the start of the emergence; Otsuji et al. 2007). Figure 5d shows a scatter plot of d_{max} and d_{unit}, which suggest that d_{unit} takes values in the range of 2–6 Mm irrespective of d_{max}. Thus, elementary and unitary Ω-loops in any emerging flux region have a common size of around 4 Mm, which is consistent with the most unstable wavelength (2–4 Mm) of the Parker instability and preceding observation/simulation studies (Magara 2001; Pariat et al. 2004; Isobe et al. 2007).

4.3.3. Magnetic flux evolution

The relation between the maximum flux, Φ_{max}, and the flux growth rate, $\langle d\Phi/dt \rangle$, is shown in figure 5e. In the scatter plot, the data points distribute along the relation

$$\left\langle \frac{d\Phi}{dt} \right\rangle = \frac{\Phi_{\mathrm{max}}}{T} = 9.6 \times 10^7 \Phi_{\mathrm{max}}^{0.57}, \tag{3}$$

where T is the emergence duration, $\langle d\Phi/dt \rangle$ is in Mx hr^{-1} and Φ_{max} in Mx. From equation (3), we can derive the emergence duration, T, in unit of hour as a function of Φ_{max}, which is

$$T = 1.03 \times 10^{-8} \Phi_{\mathrm{max}}^{0.43}. \tag{4}$$

Equation (4) indicates that an emergence event with a large maximum flux shows relatively rapid magnetic flux growth. According to equation (4), when a flux tube of Φ_0 emerges with T_0, a flux tube with $2\Phi_0$ emerges with $T_1 = 2^{0.43} T_0 \approx 1.4\,T_0$. T does not depend linearly, but non-linearly on Φ_{max}. A tube with more magnetic flux emerges in less time than in the case of a linear dependency. While equation (4) is consistent with previous observations, such as Zwaan (1987) and Hagenaar (2001), the empirical relation (4) was first derived with a wide range of magnetic parameters by Hinode high-resolution samples.

4.3.4. Relation between footpoints separating the speed and the maximum flux

Figure 5f presents the relation between Φ_{max} and $\langle v \rangle$, which indicates that larger size EFRs show a separating speed of less than $1\,\mathrm{km\,s^{-1}}$, while the small-scale EARs footpoints separate with various speeds of up to $4\,\mathrm{km\,s^{-1}}$. The mean separating speed, $\langle v \rangle$, can be written as

$$\langle v \rangle = \frac{d_{\mathrm{max}}}{T}. \tag{5}$$

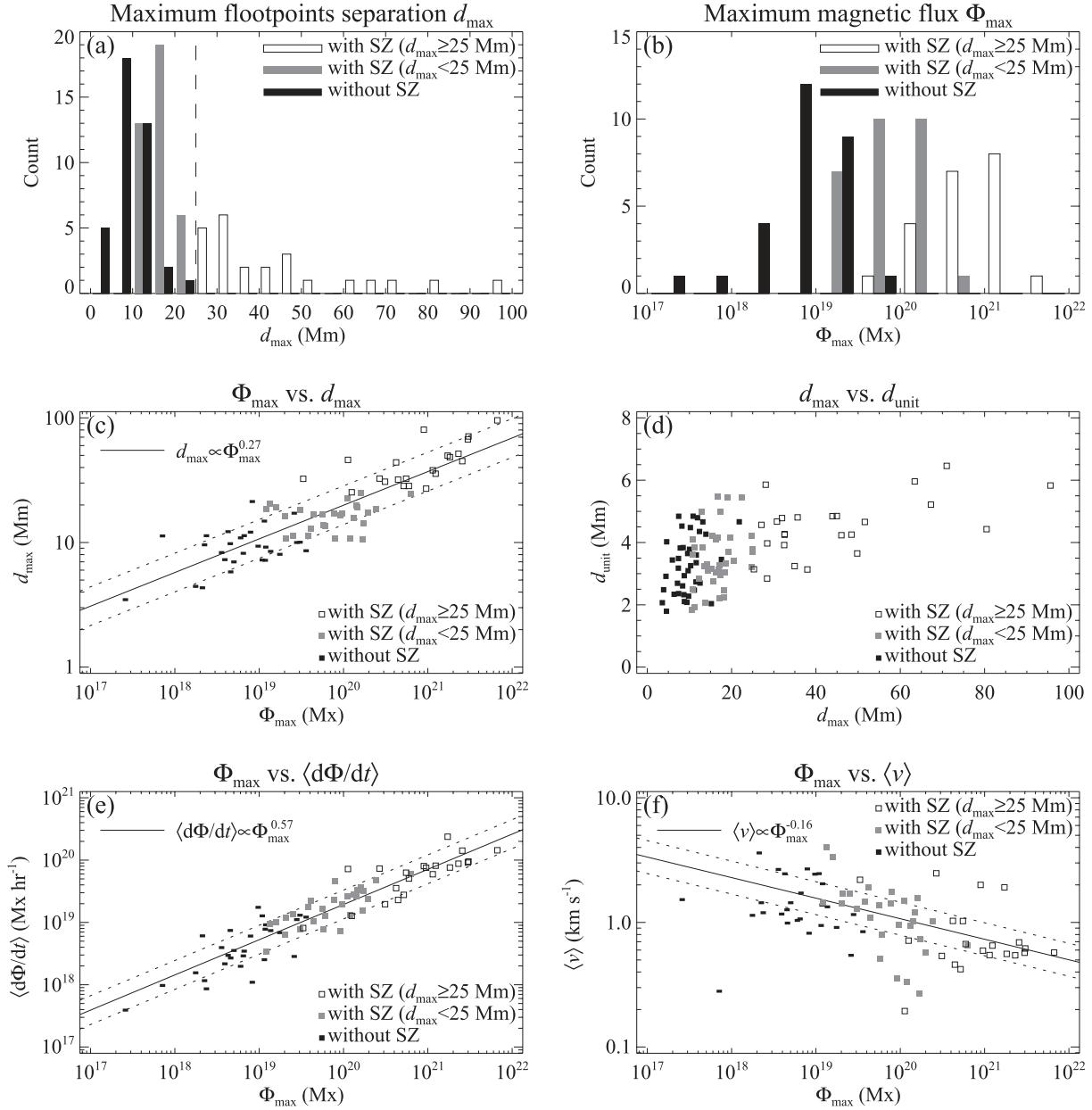From equations (2) and (4), equation (5) reduces to

Fig. 5. Statistical characteristics of magnetic flux emergences. Data points are plotted with different symbols according to the association with/without the stagnation zone (SZ). (a) Histogram of d_{max}. (b) Histogram of Φ_{max}. (c) Scatter plot of Φ_{max} and d_{max}. The solid line in the plot indicates the distribution relation of $d_{max} = 7.9 \times 10^{-5}\Phi_{max}^{0.27}$. (d) Scatter plot of d_{max} and d_{unit}. (e) Scatter plot of Φ_{max} and $\langle d\Phi/dt \rangle$. The solid line in the plot indicates the distribution relation of $\langle d\Phi/dt \rangle = 9.6 \times 10^7 \Phi_{max}^{0.57}$. (f) Scatter plot of Φ_{max} and $\langle v \rangle$. The solid line in the plot indicates the distribution relation of $\langle v \rangle = 2.1 \times 10^3 \Phi_{max}^{-0.16}$. The dashed lines in the panels represent the deviation (1σ) of the fitting plots.

$$\langle v \rangle = 2.1 \times 10^3 \Phi_{max}^{-0.16}, \qquad (6)$$

where $\langle v \rangle$ is in $\mathrm{km\,s^{-1}}$ and Φ_{max} in Mx. Equation (6) indicates that the footpoints of an emerged flux tube with less magnetic flux separate from each other with a larger speed. This relation is plotted with the solid line in figure 5e, which is consistent with the observed values.

5. Discussion

5.1. Size and Flux Dependence of SZ Formation

The SZ features are associated with a magnetic flux emergence of more than around 2×10^{19} Mx. Magara and Longcope (2003) performed a three-dimensional MHD simulation of emerging magnetic flux, and suggested that the emerging field lines take the evolutionary path of a simple expansion if they emerge with a large aspect ratio (the ratio of their height to
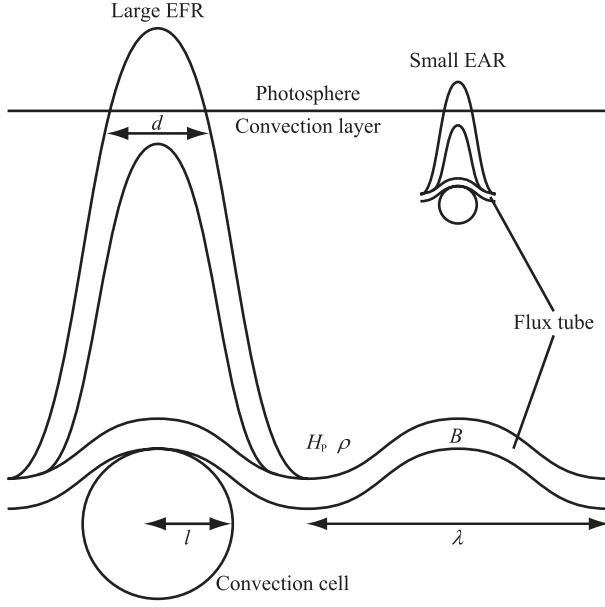
Fig. 6. Schematic image of emerging flux tubes; d is the distance between the main spots, l the mixing length, H_P the pressure scale height at the initial depth, B the field strength in the flux tube, ρ the mass density around the flux tube, and λ the most unstable wavelength of the Parker instability.

their footpoint distance); otherwise, field lines are inhibited from expanding, and they show an undulating behavior (i.e., SZ formation). Our results provide a new criterion of the total magnetic flux regarding the formation of SZs.

5.2. Flux Dependence of the Spatial Size of Flux Emergences

Another notable result is that the flux emergence phenomena with/without SZ follow the relation between the total flux and the maximum spatial size, as described in equation (2). This relation is derived from a wider range of magnetic parameters than in previous studies (Bruzek 1967; Zwaan 1987; Harvey & Martin 1973; Harvey et al. 1975). There authors gave the result for only a narrow range of magnetic parameters. We present a comprehensive result on this relation compared to that of previous studies.

Let us try to derive a power-law relation between the maximum flux, $\Phi_{\max}$, and the maximum separation distance, $d_{\max}$,

$$d_{\max} \propto \Phi_{\max}^{\alpha_1} \qquad (7)$$

from the viewpoint of simple dimensional analysis. Figure 6 shows a schematic image of flux emergence from the convection layer. First, $d_{\max}$ is estimated as follows. Initially a horizontal flux tube in the convection layer will rise with a typical length of $\lambda = 10 \sim 20\,H_P$, where H_P is the local pressure scale height. The maximum separation distance, $d_{\max}$, between two main spots depends on the most unstable wavelength of the Parker instability, λ, at the initial depth of the flux tube,

$$d_{\max} \propto \lambda \propto H_P. \qquad (8)$$

Thus, $d_{\max}$ is proportional to H_P at the depth where initially the flux tube is located.

Next, the total flux, $\Phi_{\max}$, is estimated as follows. From equipartition arguments, the magnetic and kinetic energy in the solar convection layer will balance each other,

$$\frac{B^2}{8\pi} \simeq \frac{1}{2}\rho v_{\mathrm{conv}}^2, \qquad (9)$$

where B, ρ, and v_{conv} are the field strength inside the flux tube, the mass density around the flux tube and the mean convection velocity. From mixing length theory (Stix 1989), v is given as

$$v_{\mathrm{conv}} \propto \sqrt{H_P}. \qquad (10)$$

From equations (9) and (10),

$$B \propto \sqrt{\rho H_P}. \qquad (11)$$

Now we assume that the solar convection layer can be approximated by an adiabatically stratified atmosphere (Foukal 2004),

$$T \propto \rho^{\gamma - 1}. \qquad (12)$$

T and γ are the temperature and the adiabatic index, $\gamma = c_P/c_V$, where c_P and c_V are the specific heats at constant pressure and volume, respectively. The local scale height, H_P, is proportional to the temperature, T, and thus

$$\rho \propto T^{\frac{1}{\gamma-1}} \propto H_P^{\frac{1}{\gamma-1}}. \qquad (13)$$

From equations (11) and (13),

$$B \propto H_P^{\frac{\gamma}{2(\gamma-1)}}. \qquad (14)$$

Let us think about the flux-tube width, w. If the w is much larger or smaller than the local mixing length, $l \propto H_P$, the flux tube will be disintegrated by the convection flows or accumulated at the convection boundary. Thus, the flux tube-width is expected to be comparable to the mixing length,

$$w \sim l \propto H_P. \qquad (15)$$

Thus, the total flux, $\Phi_{\max}$, can be estimated as

$$\Phi_{\max} \sim w^2 B \propto H_P^{\frac{5\gamma-4}{2(\gamma-1)}}. \qquad (16)$$

From equations (8) and (16),

$$d_{\max} \propto \Phi_{\max}^{\frac{2(\gamma-1)}{5\gamma-4}}. \qquad (17)$$

Thus, the power-law index of the relation between the maximum flux, $\Phi_{\max}$, and the maximum separation distance, $d_{\max}$, is derived to be $\alpha_1 = 2(\gamma-1)/(5\gamma-4)$. For example, α_1 is 0.30 with adiabatic index $\gamma = 5/3$ (ideal gas case realised in deep convective layers). With $\gamma \sim 4/3$ at near the solar surface, where the ionization status is changing rapidly (Bhatnagar & Livingston 2005), α_1 is 0.25. These calculated values are comparable to the observed value, $\alpha_1 = 0.27$. From the above argument, we get a view of the emergence depicted as in figure 6. Magnetic tubes of large flux are anchored in deep layers, and appear with large separation between two main spots on the solar photosphere.

5.3. Flux Growth Rate

We derived the relation between the maximum flux, $\Phi_{\max}$, and the flux growth rate, $\langle d\Phi/dt \rangle$, to be equation (3).
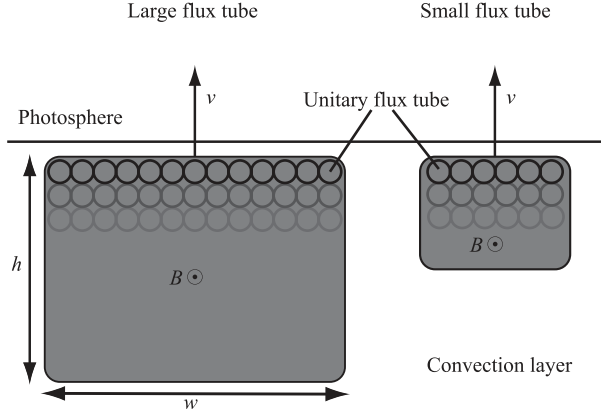
Large flux tube   Small flux tube

Fig. 7. Schematic image of a flux tube underneath the solar photosphere. The gray areas represent the cross-section of flux tubes with a field strength of B; w and h are the horizontal and vertical width of the flux tube, respectively; v is the rise velocity of the flux tubes at the photosphere. Small circles in the flux tube represent unitary and elementary flux tubes described in sub-subsection 4.3.2.

By a simple model of an emerging tube with uniform magnetic flux density, let us try to derive the power-law relation between the maximum flux and the flux growth rate,

$$\langle d\Phi/dt \rangle \propto \Phi_{\max}^{\alpha_2}. \tag{18}$$

Figure 7 shows a schematic image of the flux tubes just beneath the photosphere. Around the photosphere, the plasma β is almost 1. Thus, the magnetic pressure is $B^2/8\pi \sim P = \text{const.}$, where P is the gas pressure at the photosphere. We can thus think that the flux densities are nearly constant, irrespective of the spatial size or total flux of the magnetic tube,

$$B = \text{const.} \tag{19}$$

The rise velocity, v, of the flux tube is estimated as follows. When the apex of flux tube reaches to underneath the solar surface, the rise motion is suppressed and the tube top becomes flattened (Magara 2001). Our observation (sub-subsection 4.3.2) showed that the emergence occurs in unitary form irrespective of the total magnetic flux. In these situations the rise velocity, v, from the photosphere will not depend upon the total magnetic flux of the tube,

$$v = \text{const.} \tag{20}$$

Assuming that the aspect ratio of flux tube width, h/w, is constant just beneath the photosphere,

$$\frac{h}{w} = \text{const.}, \tag{21}$$

where w and h are horizontal and vertical width of the flux tube, respectively.

The flux growth rate and the total flux are described as

$$\langle d\Phi/dt \rangle = wvB \propto w, \tag{22}$$

$$\Phi_{\max} = whB \propto wh \propto w^2, \tag{23}$$

respectively. From equations (22) and (23), the relation between $\Phi_{\max}$ and $\langle d\Phi/dt \rangle$ is written as

$$\langle d\Phi/dt \rangle \propto \Phi_{\max}^{\frac{1}{2}}. \tag{24}$$

Thus, the power-law index is

$$\alpha_2 = 0.5, \tag{25}$$

which is consistent with the observed value of 0.57.

In this discussion we have not considered the factors such as magnetic field stratification inside the flux tube, realistic aspect ratio of tube and so on. If we include these factors then we can get more realistic interpretation of equation (3).

6. Summary

We investigated the morphological, dynamical and magnetical characteristics of various flux emergence phenomena using high-resolution Hinode SOT data. To estimate the magnetic field density of SOT data we used SOHO MDI magnetogram data for the calibration. From 101 samples of flux emergence events, we derived the total flux, flux growth rate, maximum separation and mean separation speed. The SZ features are associated with a magnetic flux emergence of more than around $2 \times 10^{19}\,\mathrm{Mx}$. The magnetic flux growth rate, emergence duration and mean separation speed were found to follow power-law functions of the total magnetic flux with indices of 0.57, 0.43, and -0.16, respectively. The typical size of elementary emergence structures is around $4\,\mathrm{Mm}$, which is consistent with the most unstable wavelength (2–4 Mm) of the Parker instability. The mean separating speed, $\langle v \rangle$, decreases with a larger magnetic flux.

We obtained a physical view of the solar flux emergence in which the emerging magnetic fields float and evolve balancing to the surrounding turbulent atmosphere from the discussion on the observed power-law relations. These observational results should be verified by future numerical studies. A possible influence of a twisting or pre-existing magnetic field could be studied with data of the horizontal magnetic field in the emerging site, which will be reported in the near future.

Appendix. Measured Quantities

Table 1. Measured quantities of 101 samples.[*]

#	Date	$d_{\max}$	$\langle v \rangle$	$\Phi_{\max}$	$\langle d\Phi/dt \rangle$	SZ	#	Date	$d_{\max}$	$\langle v \rangle$	$\Phi_{\max}$	$\langle d\Phi/dt \rangle$	SZ
1	20061126	15.2	0.97	1.2×10^{19}	2.6×10^{18}	N	51	20080807	7.4	1.87	—	—	N
2	20061201	71.0	0.62	3.0×10^{21}	9.5×10^{19}	Y	52	20080809	3.9	3.09	—	—	N
3	20061209	16.6	0.36	9.2×10^{19}	7.1×10^{18}	Y	53	20081014	12.2	1.07	—	—	Y
4	20061226	24.9	0.74	—	—	Y	54	20081018	7.5	1.20	3.9×10^{18}	2.3×10^{18}	N
5	20070104	17.4	0.58	2.0×10^{20}	2.4×10^{19}	Y	55	20081019	8.4	1.09	6.5×10^{18}	3.0×10^{18}	N
6	20070117	17.3	0.26	—	—	Y	56	20090118	14.3	0.73	1.7×10^{20}	3.2×10^{19}	Y
7	20070204	10.7	0.33	1.2×10^{20}	1.3×10^{19}	Y	57	20090226	17.6	0.56	2.6×10^{19}	3.0×10^{18}	N
8	20070205	19.2	1.21	1.5×10^{20}	3.3×10^{19}	Y	58	20090314	10.9	1.45	—	—	N
9	20070213	7.2	1.47	5.0×10^{18}	3.7×10^{18}	N	59	20090402	8.8	0.86	3.6×10^{19}	1.3×10^{19}	N
10	20070219	8.5	2.72	3.6×10^{18}	4.1×10^{18}	N	60	20090426	18.5	1.44	1.2×10^{19}	3.4×10^{18}	Y
11	20070308	16.8	1.38	5.7×10^{19}	1.7×10^{19}	Y	61	20090601	32.6	2.48	2.7×10^{20}	7.3×10^{19}	Y
12	20070328	7.8	0.29	—	—	N	62	20090603	30.7	0.54	3.1×10^{20}	2.0×10^{19}	Y
13	20070331	11.6	1.76	6.6×10^{18}	3.6×10^{18}	N	63	20090623	7.4	2.52	1.1×10^{19}	1.3×10^{19}	N
14	20070414	10.7	1.70	2.1×10^{19}	1.2×10^{19}	Y	64	20090704	63.4	0.35	—	—	Y
15	20070419	16.7	1.09	4.5×10^{19}	1.0×10^{19}	Y	65	20090707	51.6	0.54	2.3×10^{21}	8.8×10^{19}	Y
16	20070601	15.3	0.50	—	—	Y	66	20090821	5.9	1.01	4.6×10^{18}	2.8×10^{18}	N
17	20070603	14.2	0.73	—	—	Y	67	20090928	10.2	1.18	2.8×10^{19}	1.2×10^{19}	N
18	20070702	8.2	0.93	1.8×10^{19}	7.2×10^{18}	N	68	20091009	9.8	1.47	2.3×10^{18}	1.2×10^{18}	N
19	20070807	32.0	0.46	4.4×10^{20}	2.3×10^{19}	Y	69	20091015	9.4	2.09	1.2×10^{19}	9.6×10^{18}	N
20	20070825	12.9	1.90	4.2×10^{19}	2.2×10^{19}	Y	70	20091019	10.0	1.29	4.5×10^{18}	7.8×10^{18}	N
21	20070918	9.6	2.49	9.7×10^{18}	1.8×10^{19}	N	71	20091023	34.9	0.44	—	—	Y
22	20070929	20.6	3.99	1.3×10^{19}	9.4×10^{18}	Y	72	20091025	9.7	1.00	—	—	N
23	20071001	22.5	1.48	1.1×10^{20}	2.7×10^{19}	Y	73	20091026	49.8	1.91	1.7×10^{21}	2.4×10^{20}	Y
24	20071008	11.2	1.70	2.5×10^{19}	1.4×10^{19}	Y	74	20091207	11.2	1.06	6.0×10^{18}	2.1×10^{18}	N
25	20071009	16.3	1.42	2.0×10^{19}	6.4×10^{18}	Y	75	20091215	80.5	2.00	9.0×10^{20}	8.0×10^{19}	Y
26	20071015	6.4	0.59	—	—	N	76	20091226	19.7	1.03	1.4×10^{20}	2.7×10^{19}	Y
27	20071020	8.8	0.63	—	—	N	77	20091229	32.6	1.03	5.5×10^{20}	6.3×10^{19}	Y
28	20071026	8.7	1.36	1.4×10^{19}	7.7×10^{18}	N	78	20091230	67.3	0.57	3.0×10^{21}	9.1×10^{19}	Y
29	20071108	4.4	3.69	2.1×10^{18}	6.4×10^{18}	N	79	20100108	28.4	0.67	6.0×10^{20}	5.1×10^{19}	Y
30	20071111	19.1	3.35	1.6×10^{19}	1.0×10^{19}	Y	80	20100109	45.0	0.69	2.6×10^{21}	1.4×10^{20}	Y
31	20071117	7.4	1.41	1.2×10^{19}	8.1×10^{18}	N	81	20100110	95.6	0.57	6.7×10^{21}	1.4×10^{20}	Y
32	20071123	24.8	0.63	—	—	Y	82	20100124	15.7	0.94	1.3×10^{20}	2.8×10^{19}	Y
33	20071127	12.5	2.51	4.3×10^{18}	3.1×10^{18}	N	83	20100217	25.3	0.71	1.3×10^{20}	1.3×10^{19}	Y
34	20071129	13.2	1.11	—	—	Y	84	20100221	10.7	1.75	7.9×10^{19}	4.7×10^{19}	Y
35	20071207	13.2	0.33	—	—	N	85	20100222	32.5	2.20	3.3×10^{19}	8.1×10^{18}	Y
36	20071208	35.6	0.65	1.2×10^{21}	8.1×10^{19}	Y	86	20100313	11.6	1.22	2.4×10^{18}	9.0×10^{17}	N
37	20071209	17.2	0.96	9.6×10^{19}	1.9×10^{19}	Y	87	20100322	4.5	1.17	1.8×10^{18}	1.6×10^{18}	N
38	20071210	24.9	1.56	1.6×10^{20}	3.6×10^{19}	SZ	88	20100325	11.3	1.46	3.8×10^{19}	1.8×10^{19}	SZ
39	20071211	27.1	0.59	9.5×10^{20}	7.5×10^{19}	Y	89	20100414	10.3	1.28	3.1×10^{19}	1.4×10^{19}	N
40	20071212	15.4	0.75	—	—	Y	90	20100612	46.0	0.19	1.1×10^{20}	7.2×10^{19}	Y
41	20071213	24.7	0.66	6.3×10^{20}	6.0×10^{19}	Y	91	20100613	28.1	0.65	—	—	Y
42	20080105	11.9	0.45	—	—	N	92	20100618	13.8	0.51	5.8×10^{19}	7.7×10^{18}	Y
43	20080106	13.9	1.00	—	—	N	93	20100619	38.0	0.55	1.1×10^{21}	5.9×10^{19}	Y
44	20080113	18.1	1.09	—	—	Y	94	20100723	18.5	1.03	2.4×10^{20}	4.8×10^{19}	Y
45	20080124	18.2	1.30	3.0×10^{19}	7.8×10^{18}	Y	95	20100727	13.6	0.80	6.0×10^{19}	1.3×10^{19}	Y
46	20080419	17.1	1.41	7.7×10^{19}	2.3×10^{19}	Y	96	20100728	48.4	0.56	1.8×10^{21}	7.6×10^{19}	Y
47	20080610	21.8	0.84	8.3×10^{18}	1.1×10^{18}	N	97	20100805	28.4	0.42	5.2×10^{20}	2.8×10^{19}	Y
48	20080615	16.2	0.33	—	—	Y	98	20100809	10.6	0.27	1.7×10^{20}	1.5×10^{19}	Y
49	20080620	4.6	2.08	—	—	N	99	20100812	11.6	0.29	7.1×10^{17}	1.0×10^{18}	N
50	20080630	3.6	1.56	2.6×10^{17}	4.1×10^{17}	N	100	20100814	43.9	1.03	4.2×10^{20}	3.5×10^{19}	Y
							101	20100822	12.4	2.75	7.9×10^{18}	6.3×10^{18}	N

[*] Column (1): identification number of the flux emergence. Column (2): date of the flux emergence. Column (3): maximum distance between two main spots (Mm). Column (4): mean separating speed of the main spots (km s^{-1}). Column (5): maximum flux increment (Mx). Column (6): flux growth rate (Mx hr^{-1}). Column (7): existence of stagnation zone (Yes/No). The missing value (—) is due to the event with only Ca II H observation and without magnetogram.

References

Archontis, V., & Hood, A. W. 2009, A&A, 508, 1469

Berger, T. E., Löfdahl, M. G., Shine, R. S., & Title, A. M. 1998, ApJ, 495, 973

Bernasconi, P. N., Rust, D. M., Georgoulis, M. K., & Labonte, B. J. 2002, Sol. Phys., 209, 119

Bhatnagar, A., & Livingston, W. 2005, Fundamentals of Solar Astronomy (Singapore: World Scientific Series), 374

Brants, J. J. 1985, Sol. Phys., 95, 15

Brants, J. J., & Steenbeek, J. C. M. 1985, Sol. Phys., 96, 229

Brants, J. J., & Zwaan, C. 1982, Sol. Phys., 80, 251

Bruzek, A. 1967, Sol. Phys., 2, 451

Bruzek, A. 1969, Sol. Phys., 8, 29

Centeno, R., et al. 2007, ApJ, 666, L137

Cheung, M. C. M., Rempel, M., Title, A. M., & Schüssler, M. 2010, ApJ, 720, 233

Cheung, M. C. M., Schüssler, M., Tarbell, T. D., & Title, A. M. 2008, ApJ, 687, 1373

Chou, D.-Y., & Zirin, H. 1988, ApJ, 333, 420

Ellerman, F. 1917, ApJ, 46, 298

Fan, Y. 2001, ApJ, 554, L111

Foukal, P. 2004, Solar Astrophysics (Weinheim: Wiley-VCH), 173

Guglielmino, S. L., Zuccarello, F., Romano, P., & Bellot Rubio, L. R. 2008, ApJ, 688, L111

Hagenaar, H. J. 2001, ApJ, 555, 448

Harvey, K. L., Harvey, J. W., & Martin, S. F. 1975, Sol. Phys., 40, 87

Harvey, K. L., & Martin, S. F. 1973, Sol. Phys., 32, 389

Ichimoto, K., et al. 2004, Proc. SPIE, 5487, 1142

Isobe, H., Tripathi, D., & Archontis, V. 2007, ApJ, 657, L53

Kitai, R. 1983, Sol. Phys., 87, 135

Kosugi, T., et al. 2007, Sol. Phys., 243, 3

Kurokawa, H., Kawaguchi, I., Funakoshi, Y., & Nakai, Y. 1982, Sol. Phys., 79, 77

Loughhead, R. E., & Bray, R. J. 1961, Aust. J. Phys., 14, 347

Magara, T. 2001, ApJ, 549, 608

Magara, T., & Longcope, D. W. 2001, ApJ, 559, L55

Magara, T., & Longcope, D. W. 2003, ApJ, 586, 630

Martin, S. F. 1988, Sol. Phys., 117, 243

Matsumoto, R., & Shibata, K. 1992, PASJ, 44, 167

Matsumoto, R., Tajima, T., Shibata, K., & Kaisig, M. 1993, ApJ, 414, 357

Matsumoto, T., et al. 2008b, PASJ, 60, 577

Matsumoto, T., & Kitai, R. 2010, ApJ, 716, L19

Matsumoto, T., Kitai, R., Shibata, K., Otsuji, K., Naruse, T., Shiota, D., & Takasaki, H. 2008a, PASJ, 60, 95

Murray, M. J., Hood, A. W., Moreno-Insertis, F., Galsgoard, K., & Archontis, V. 2006, A&A, 460, 909

November, L. J., & Simon, G. W. 1988, ApJ, 333, 427

Nozawa, S. 2005, PASJ, 57, 995

Nozawa, S., Shibata, K., Matsumoto, R., Sterling, A. C., Tajima, T., Uchida, Y., Ferrari, A., & Rosner, R. 1992, ApJS, 78, 267

Otsuji, K., et al. 2007, PASJ, 59, S649

Otsuji, K., Kitai, R., Matsumoto, T., Ichimoto, K., Ueno, S., Nagata, S., Isobe, H., & Shibata, K. 2010, PASJ, 62, 893

Pariat, E., Aulanier, G., Schmieder, B., Georgoulis, M. K., Rust, D. M., & Bernasconi, P. N. 2004, ApJ, 614, 1099

Parker, E. N. 1966, ApJ, 145, 811

Scherrer, P. H., et al. 1995, Sol. Phys., 162, 129

Shibata, K., Tajima, T., Steinolfson, R.S., & Matsumoto, R. 1989, ApJ, 345, 584

Shimizu, T., et al. 2007, Sol. Phys., 249, 221

Stix, M. 1989, The Sun (Heidelberg: Springer-Verlag) 198

Strous, L. H., Scharmer, G., Tarbell, T. D., Title, A. M., & Zwaan, C. 1996, A&A, 306, 947

Strous, L. H., & Zwaan, C. 1999, ApJ, 527, 435

Suematsu, Y., et al. 2008, Sol. Phys., 249, 197

Titov, V. S., Priest, E. R., & Démoulin, P. 1993, A&A, 276, 564

Tsuneta, S., et al. 2008, Sol. Phys., 249, 167

Watanabe, H., et al. 2008, ApJ, 684, 736

Zirin, H. 1972, Sol. Phys., 22, 34

Zwaan, C. 1987, Annu. Rev. Astron. Astrophys., 25, 83

Zwaan, C., Brants, J. J., & Cram, L. E. 1985, Sol. Phys., 95, 3